

Confined Liquid-Phase Growth of Crystalline Compound Semiconductors on Any Substrate

Debarghya Sarkar,[†] Wei Wang,[†] Matthew Mecklenburg,[‡] Andrew J. Clough,^{‡,§} Matthew Yeung,^{||} Chenhao Ren,[†] Qingfeng Lin,[†] Louis Blankemeier,[†] Shanyuan Niu,[⊥] Huan Zhao,[†] Haotian Shi,[§] Han Wang,[†] Stephen B. Cronin,[†] Jayakanth Ravichandran,[⊥] Mitul Luhar,[#] and Rehan Kapadia^{*,†}

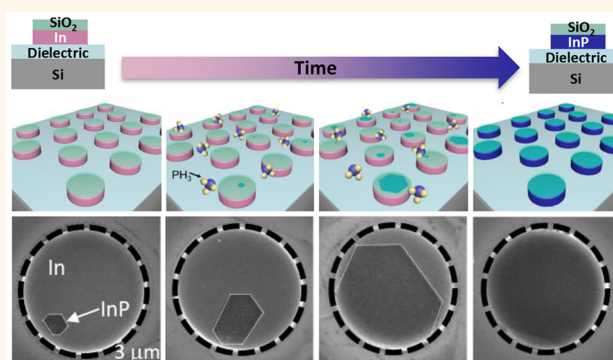
[†]Ming Hsieh Department of Electrical Engineering, [‡]Center for Electron Microscopy and Microanalysis, [§]Department of Chemistry, [⊥]Mork Family Department of Chemical Engineering and Materials Science, and [#]Department of Aerospace and Mechanical Engineering, University of Southern California, Los Angeles, California 90089, United States

^{||}Molecular Foundry, Lawrence Berkeley National Laboratory, One Cyclotron Road, Berkeley, California 94720, United States

Supporting Information

ABSTRACT: The growth of crystalline compound semiconductors on amorphous and non-epitaxial substrates is a fundamental challenge for state-of-the-art thin-film epitaxial growth techniques. Direct growth of materials on technologically relevant amorphous surfaces, such as nitrides or oxides results in nanocrystalline thin films or nanowire-type structures, preventing growth and integration of high-performance devices and circuits on these surfaces. Here, we show crystalline compound semiconductors grown directly on technologically relevant amorphous and non-epitaxial substrates in geometries compatible with standard microfabrication technology. Furthermore, by removing the traditional epitaxial constraint, we demonstrate an *atomically sharp lateral heterojunction* between indium phosphide and tin phosphide, two materials with vastly different crystal structures, a structure that cannot be grown with standard vapor-phase growth approaches. Critically, this approach enables the growth and manufacturing of crystalline materials without requiring a nearly lattice-matched substrate, potentially impacting a wide range of fields, including electronics, photonics, and energy devices.

KEYWORDS: templated liquid-phase growth, non-epitaxial crystalline compound semiconductors, controlled wetting of liquid metals, phase-controlled and far-from-equilibrium growth, lateral heterojunction



Nearly all non-silicon integrated electronic^{1,2} and photonic^{3,4} devices are manufactured using epitaxial growth techniques. Fundamental to either liquid- or vapor-phase epitaxy is the necessity of an epitaxial substrate, which prevents growth of high-quality crystalline materials on amorphous and non-epitaxial substrates. This limitation has severely restricted the development of high-performance materials for applications such as multilevel logic devices, growth of electronic and photonic devices directly on silicon, and electronics on substrates such as glass and plastics. To address this challenge, two classes of techniques have been previously developed: (i) nanomaterial growth and device fabrication^{5–8} and (ii) epitaxial transfer.^{9–12} Nanomaterial growth is typically carried out using a nanoscale catalyst on an arbitrary substrate, creating high-quality nanowires but without the necessary control over the geometry and position of materials, often resulting in vertical nanowires which are not compatible with traditional silicon fabrication. Epitaxial transfer, where a high-quality material is first grown on a lattice-matched

wafer with a sacrificial layer, followed by transfer of the crystalline semiconductor layers onto active substrates, has also been successful. Although this approach has enabled high-performance devices on nearly any substrate, the cost and scalability challenges have limited the overall applicability. Recently, growth of indium phosphide crystals on non-epitaxial substrates was demonstrated through the templated liquid-phase (TLP) growth process.¹³ However, successful templating of a liquid metal required the use of a metal^{14–16} or a substoichiometric MoO_x^{13,17,18} wetting layer on which materials are grown. Both surfaces are unsuitable for a general growth technique, due to issues with shorting lateral devices and instability, respectively. Thus, a general growth technique for crystalline materials on amorphous and non-epitaxial substrates is still a need.

Received: March 10, 2018

Accepted: May 18, 2018

Published: May 18, 2018

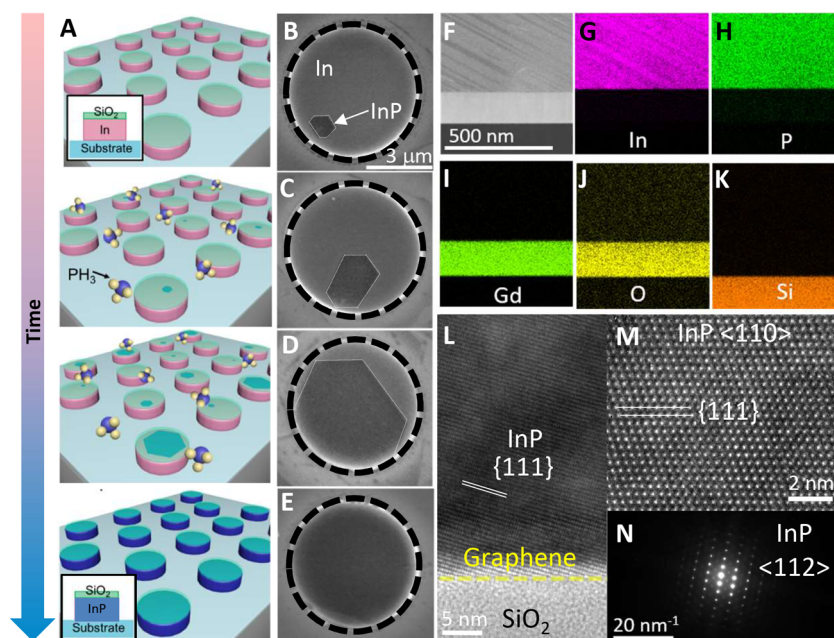


Figure 1. Overview of TLP growth of crystalline compound semiconductors on any substrate. (A) Schematic of the TLP growth process. (B–E) SEM image of InP growing in an indium template on a Gd_2O_3 substrate. (F) TEM image of InP on $\text{Gd}_2\text{O}_3/\text{Si}$. (G–K) Corresponding EDS maps of In, P, Gd, O, and Si. (L) TEM image of InP grown on graphene transferred to a Si/SiO_2 wafer. (M) High-resolution TEM image of InP grown on TiO_2 . (N) Selected area electron diffraction pattern of InP.

Here, we show that constrained wetting of liquid metals on any substrate enables a general growth technique for the growth of crystalline materials on amorphous and non-epitaxial substrates. By first deriving a *wetting phase diagram* for templated liquid metals, we show that there exist multiple classes of templating behavior for relevant materials. Critically, we find that a geometrically driven wetting condition exists for any substrate surface energy. With this, we then show that InP, GaP, InAs, InGaP, SnP, and Sn_4P_3 crystals can be grown directly on SiO_2 , Si_3N_4 , TiO_2 , Al_2O_3 , Gd_2O_3 , SrTiO_3 , and graphene. The variety of materials and substrates illustrates this approach is truly general. Optoelectronic characterization of the InP shows excellent characteristics despite it being directly grown on oxides and nitrides. Finally, it is shown that TLP enables atomically sharp lateral interfaces between materials with vastly different crystal structures, with potential applications in next generation interfaces and devices.

RESULTS AND DISCUSSION

First, we introduce a *generalized* TLP growth technique for crystal growth on any substrate, regardless of epitaxial relation. Figure 1A shows a schematic of the TLP process, with details in the *Methods* section. Briefly, a metal with a capping oxide layer is deposited in the desired template geometry and pattern on a substrate with standard evaporation or sputtering techniques. The substrate is then heated in H_2 , causing the metal to melt. For this approach to create usable materials, the liquid must remain in the original deposited geometry. If dewetting occurs, the resulting growths are unusable (Figure S1). At the growth temperature, a precursor gas is introduced, causing supersaturation and precipitation of the target material. Unlike vapor-phase growth techniques, where thin films grow from numerous nucleation sites on a substrate, in TLP, the precursor flux can be controlled so that a single nucleus¹³ forms in each template. As this nucleus grows, the liquid metal is consumed,

leaving behind a single crystal in the geometry of the template. Figure 1B–E shows the scanning electron microscopy (SEM) images of TLP growth of InP in an indium template at various stages of growth, starting with a single nucleus of the thermodynamically favorable hexagonal faceted shape for a (111)-oriented crystal and ending with the circular template geometry.

To understand the nature of the interface between the single-crystal templates and the substrate, as well as the structural quality of the materials, we have carried out transmission electron microscopy (TEM) imaging of InP/ $\text{Gd}_2\text{O}_3/\text{Si}$, InP/graphene/ SiO_2/Si , and InP/ $\text{TiO}_2/\text{SiO}_2/\text{Si}$. Figure 1F shows a TEM image of InP grown on a $\text{Si}/\text{Gd}_2\text{O}_3$ substrate, and Figure 1G–K shows the corresponding energy-dispersive spectrometry (EDS) maps of In, P, Gd, O, and Si. Critically, the EDS images (Figure 1G–K) indicate that the InP has a clean boundary with the underlying Gd_2O_3 substrate. Figure 1L shows a TEM image of InP/graphene/ SiO_2/Si , where the lattice planes of InP are clearly visible. This indicates both the crystalline nature of the InP and the clean interface with the substrate. Finally, we show a scanning transmission electron microscope (STEM) image of an InP crystal grown on a TiO_2 substrate (Figure 1M), with the atomic resolution showing the excellent crystalline quality of materials grown *via* this approach. The electron diffraction pattern of the crystal along the $\langle 112 \rangle$ zone axis is shown in Figure 1N. Preventing breakup of the liquid metal film in the template is the critical challenge in TLP. To date, this has been achieved by using indium on Mo or MoO_x substrates with an SiO_x cap,^{13–17} which allows complete wetting of the template surface due to favorable surface energies. On most other substrates, the liquid metal films tend to dewet, leaving behind uncontrolled liquid droplets which are not useful for devices (representative dewetted InP growth on Gd_2O_3 is shown in Figure S1). Thus, the development of a model for microscale template wetting is critical. Here, we first experimentally study the behavior of

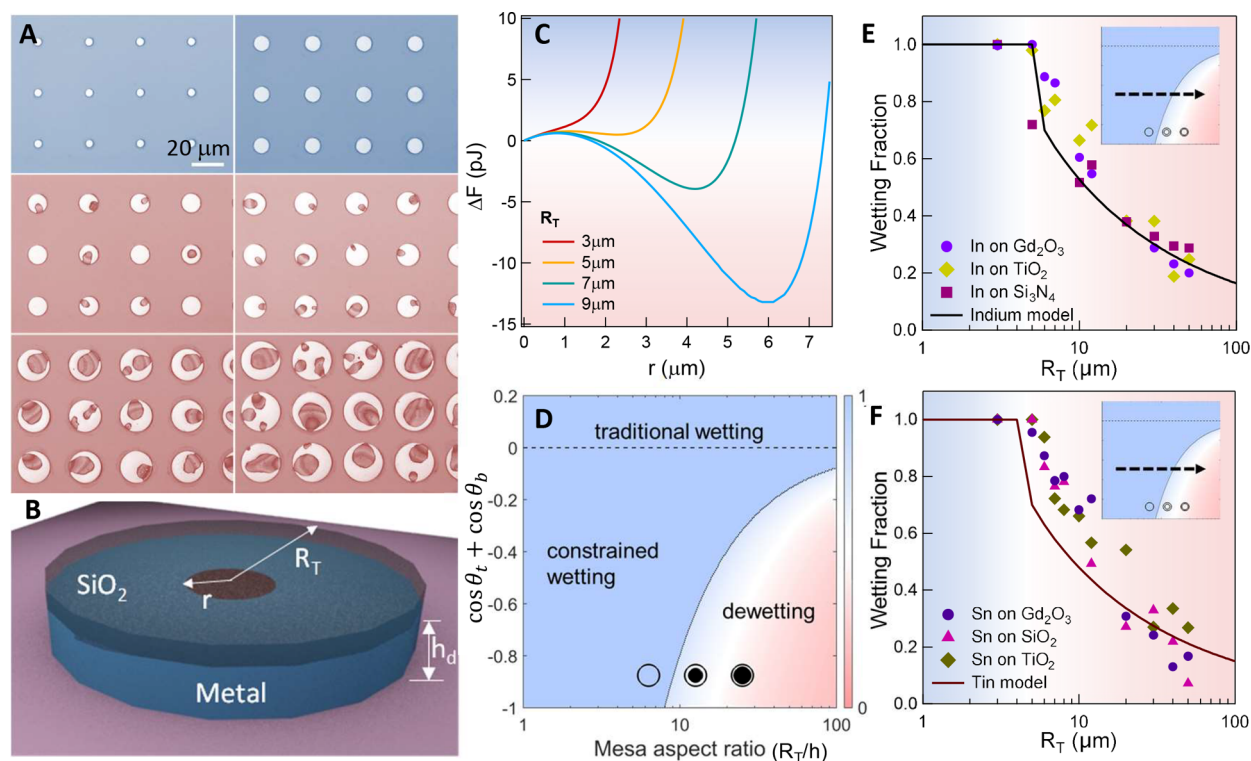


Figure 2. Wetting characteristics of liquid metal templates on any substrate. (A) Experimental wetting–dewetting of indium templates on Gd_2O_3 substrate. (B) Schematic of dewetted model template with radius R_T , void radius r , and height h_d . (C) Calculated free energy of formation for a void of radius r in different microscale liquid templates of radii R_T . (D) Wetting phase diagram showing traditional wetting (surface energy driven), constrained wetting (geometry driven), and dewetting regimes. Color bar: wetting fraction. (E) Model and experimental data for indium on multiple substrates. (F) Model and experimental data for tin on multiple substrates.

circular indium templates on an oxide surface (representative image shown in Figure S2) as they are heated to $250\text{ }^\circ\text{C}$ in vacuum ($T_{\text{melt}} = 157\text{ }^\circ\text{C}$) and then cooled to room temperature. Figure 2A shows the result for 400 nm thick indium templates with a SiO_x capping layer on a Gd_2O_3 substrate. Two behaviors were observed. First, below a critical template radius, there was no observable dewetting, whereas above the radius, nearly all templates dewetted. Second, for the templates which dewetted, there is a stable void size in the dewetted films. We have developed a thermodynamic model (eq 1, derived in the Supporting Information) that can explain these results and can also predict both observed behaviors. We calculated the change in free energy of a liquid metal template of height h as a function of void radius r and template radius R_T to evaluate the propensity for dewetting (illustrated schematically in Figure 2B).

$$\begin{aligned} \Delta F &= (F_{\text{dewetting}} - F_{\text{wetting}}) \\ &= \pi r^2(\sigma_{\text{tv}} - \sigma_{\text{tl}} + \sigma_{\text{bv}} - \sigma_{\text{bl}}) + 2\pi R_T h \left(\frac{r}{R_T - r} \right) \sigma_{\text{lv}} \end{aligned} \quad (1)$$

Here, σ_{tl} is the surface energy between top capping layer material and liquid metal; σ_{bl} is the surface energy between bottom substrate material and liquid metal; σ_{lv} is the surface energy between liquid metal and vapor; σ_{tv} is the surface energy between top capping layer material and vapor; σ_{bv} is the surface energy between bottom substrate material and vapor. Figure 2C shows ΔF for 400 nm thick In on a Gd_2O_3 surface and a SiO_2 capping layer with differing template radii, R_T . Importantly, we

see that the behavior of the free energy curves predicts that below a critical template radius, void formation in the film is energetically unfavorable ($\Delta F > 0$ for all r), and that above the critical radius, there exists a minimum in the free energy ($d\Delta F/dr = 0$), indicating a thermodynamically favorable void size. Figure 2D shows a “wetting phase diagram”, with the horizontal axis corresponding to the template aspect ratio (R_T/h) and the vertical axis corresponding to the sum of the contact angles, $\cos \theta_t + \cos \theta_b \left(= \frac{\sigma_{\text{tv}} - \sigma_{\text{tl}}}{\sigma_{\text{lv}}} + \frac{\sigma_{\text{bv}} - \sigma_{\text{bl}}}{\sigma_{\text{lv}}} \right)$, where θ_t is the contact angle between the liquid metal and the capping material and θ_b is the contact angle between the liquid metal and the substrate. When this sum is greater than 0, the surface energies of the template prevent the formation of a stable void, independent of the template geometry. When this sum is less than zero, the liquid wets the template only when it is below some critical aspect ratio, $(R_T/h)_{\text{crit}}$. Therefore, nearly independent of surface energy, it is possible to find dimensions which enable wetting of the template and thus allows us to carry out confined liquid-phase growth on any thermally stable substrate. Figure 2E shows the wetting fraction, defined as $1 - A_{\text{void}}/A_{\text{template}}$ (i.e., unity wetting fraction indicates no void), for a 400 nm thick indium template as a function of template radius. For templates with a radius less than $6\text{ }\mu\text{m}$, no stable void can form, and thus no dewetting occurs. Larger templates support a stable void, and thus the wetting fraction falls below 1. Figure 2F shows the same behavior with tin. The model developed here shows excellent agreement with experimental data. Optical microscope images of the In and Sn templates of different radii after the dewetting experiment are shown in Figures S3 and S4, respectively. This allows us to predict and design templates that

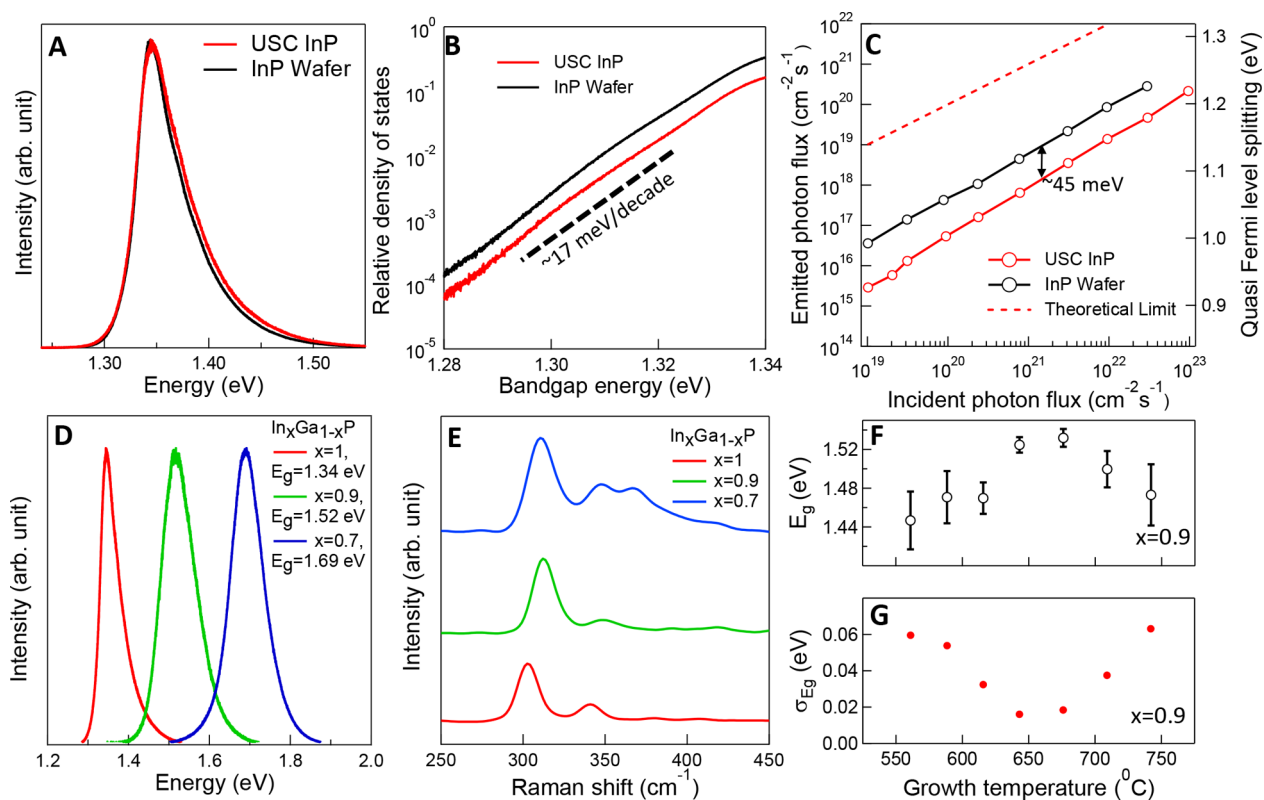


Figure 3. Optoelectronic characterization of InP and InGaP. (A) Photoluminescence spectra of a commercial InP wafer and the USC InP. (B) Sub-band-gap density of spectra states. (C) Quantitative photoluminescence of USC InP and InP wafer. (D) PL spectra and (E) Raman spectra of InGaP with varying Ga fractions. (F) Extracted band gap and dispersion in observed band gap across grown $\text{In}_{0.9}\text{Ga}_{0.1}\text{P}$ as a function of temperature. (G) Standard deviation of band gap across growths as a function of temperature.

will enable liquid-phase wetting on a substrate of choice with knowledge of only the surface energy values. Notably, a similar dewetting experiment on MoO_x gives unity wetting fraction irrespective of the template radius, shown in Figure S5, thus further validating the experimental procedure and the theoretical model.

After establishing liquid metal wetting on any substrate, we study the optoelectronic quality of the materials grown on various substrates. While the crystallinity is easily observable from direct inspection, such as TEM or visual observation of the crystal geometry while growing, understanding the quality of this material requires more sensitive probes. Steady-state photoluminescence (PL) curves of the TLP InP on Gd_2O_3 and a commercially purchased InP wafer are shown in Figure 3A, with spectra on other substrates shown in Figure S6. Both the peak position (1.34 eV) and full width at half-maxima (50 meV) are identical, indicating good quality of the grown material. Brief statistics of the quality metrics are given in Table S1. A more sensitive probe of the material quality is the sub-band-gap absorption or band tail,¹⁹ which is heavily influenced by disorder in the semiconductor. Sharper band tails are indicative of higher electronic quality and are defined by a smaller inverse slope in units of meV/decade. The absorption coefficient is related to the photoluminescence²⁰ via eq 2 (see Methods for details), which can be fit with an exponential relation at the band edge with an energy rate factor, E_0 , called the Urbach parameter.²¹

$$\alpha(\nu) \propto \frac{P(\nu)(e^{h\nu/kT} - 1)}{\nu^2} \propto e^{h\nu - E_{\text{ref}}/E_0} \quad (2)$$

Here, the TLP InP exhibits a band tail slope of 17.18 meV/decade with $E_0 = 7.16$ meV, and the InP wafer exhibits a slightly higher 17.38 meV/decade with $E_0 = 7.34$ meV (Figure 3B).

The most sensitive probe of optoelectronic quality, however, is the photoluminescence efficiency, which enables us to extract the electron and hole quasi-Fermi level splitting in a material. Figure 3C shows the photoluminescence efficiency and quasi-Fermi level splitting (ΔE_F) versus incident power for TLP and commercial InP (see Methods for process details). ΔE_F is defined as the difference between the electron and hole quasi-Fermi level under illumination. The dashed line indicates ΔE_F for the ideal case, where only radiative emission processes exist, and every absorbed photon is re-emitted as photoluminescence. Critically, within the range of measured photon fluxes, the difference in ΔE_F between the grown InP and wafer is ~ 45 meV. Compared to the theoretical limit, the InP wafer is $\Delta E_F \sim 150$ meV lower, and the TLP InP exhibits ~ 195 meV less than the theoretical limit. Thus, we show this approach enables the growth of excellent quality materials with spectral characteristics, sub-band-gap absorption, and luminescence intensity nearly identical to that of single-crystalline wafers. The applicability of TLP to previously studied metal substrates has also been demonstrated by InP and InAs growth on Mo substrate (Figure S7).

A key advantage of III–V material systems is the tunability of the band gap via alloying of multiple group III or group V elements. Unlike binary line compounds such as InP or GaP, alloys have a wide range of stable stoichiometries; therefore, ensuring uniform alloy composition during growth is a challenge. For TLP growth of an $\text{In}_x\text{Ga}_{1-x}\text{P}$ alloy, the approach

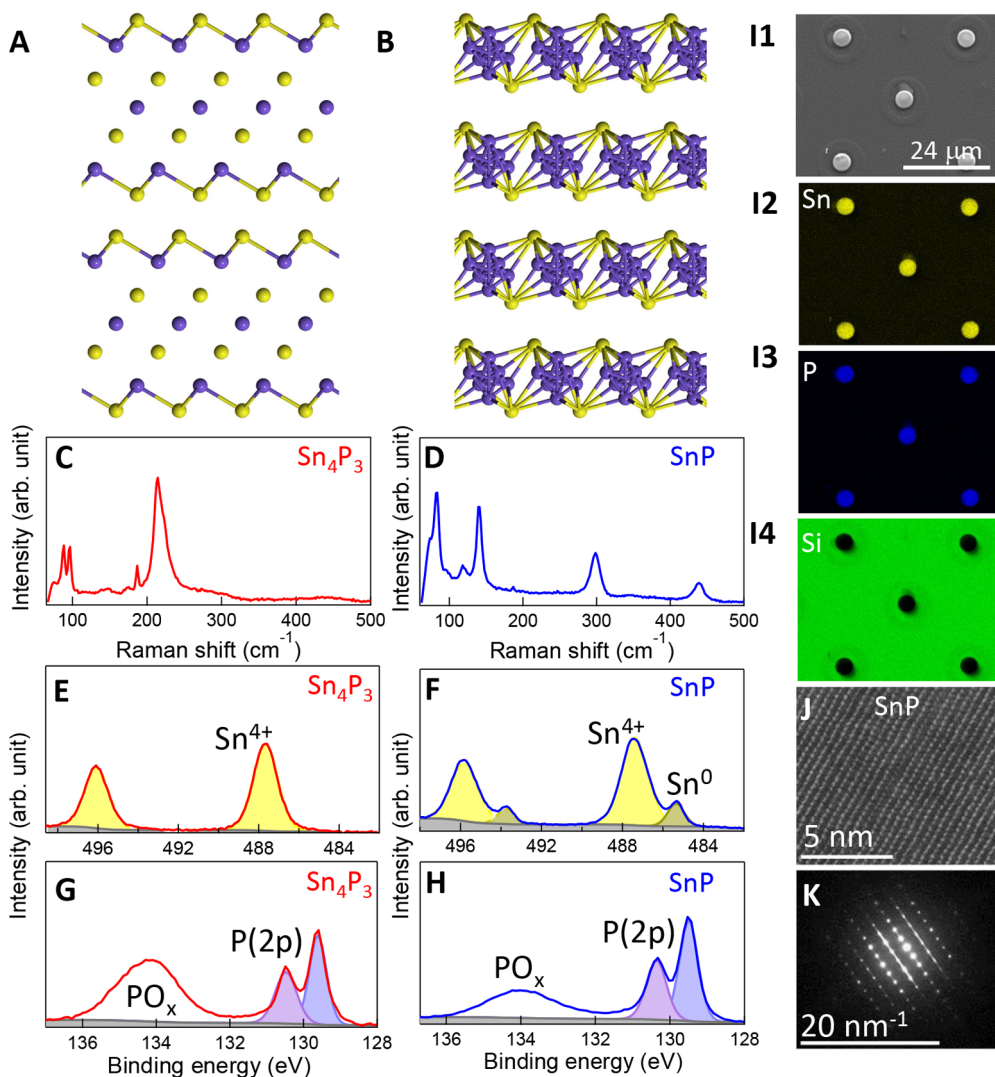


Figure 4. Phase-controlled growth of single-crystalline tin phosphide templates. Crystal structure of (A) Sn_4P_3 and (B) SnP . (C,D) Raman spectra. (E,F) $\text{Sn}(3d)$ XPS spectra. (G,H) $\text{P}(2p)$ XPS spectra. (I1) SEM image of tin phosphide on SiO_2/Si . (I2–I4) Corresponding EDS maps of Sn, P, and Si. (J) High-resolution TEM image and (K) selected area electron diffraction of SnP .

would be to evaporate In and Ga as the template with the desired atomic ratio and then carry out the growth. With a near equilibrium liquid-phase growth approach, however, uniform material can only be achieved if the solid which precipitates out has the same In/Ga ratio as the liquid. However, in general, the solid will not have the same In/Ga ratio as the liquid, and thus we would not expect to be able to create uniform materials. Thus, the composition of the liquid would continuously change throughout the growth process, resulting in significant lateral grading of the solid composition and band gap. This would be observable as a large spread in the peak position of the photoluminescence.²²

To explore this, circular $\text{In}_x\text{Ga}_{1-x}$ templates with $x = 1, 0.9, 0.7,$ and 0 were fabricated and then grown under a phosphine/hydrogen ambient environment at temperatures varying from 550 to 750 °C. After growth, the results were interrogated through microphotoluminescence, with a spot diameter of 1 μm . Figure 3D shows photoluminescence of the $\text{In}_x\text{Ga}_{1-x}\text{P}$ grown by tuning the In/Ga ratio in the template.²³ In Figure 3E, we show how the Raman spectra of the grown material shift as a function of In/Ga ratio. The TO and LO peaks of InP shift as Ga is added,²⁴ and at higher Ga fractions ($x = 0.7$), we see

the emergence of a third, broader GaP-like LO peak, induced by alloy disorder. The GaP Raman spectrum is shown in Figure S8.

Although the micro-PL shows that tuning the composition of the liquid metal clearly changes the band gap of the grown material, it is necessary to identify the spread in band gap to quantify the results of the growth. By taking multiple PL spectra across a grown chip and extracting the peak energy, the spread in band gap is determined. $\text{In}_{0.9}\text{Ga}_{0.1}\text{P}$ was grown at temperatures ranging from 550 to 750 °C, with Figure 3F showing the peak position with error bars representing the distribution, and Figure 3G shows the standard deviation of the peak position. A minimum in the standard deviation of the material is observed for a growth temperature of 645 °C of 16 meV, which is significantly lower than expected. Thus, the uniformity of this material is expected to be driven by growth at a high rate, pushing it far from equilibrium and removing the expected constraint due to near equilibrium growth. The experimental trend is consistent with this hypothesis. At lower temperatures, the growth rate is limited by the precursor cracking and mass transport to the substrate, whereas, at higher temperatures, the growth rate is reduced due to an increase in

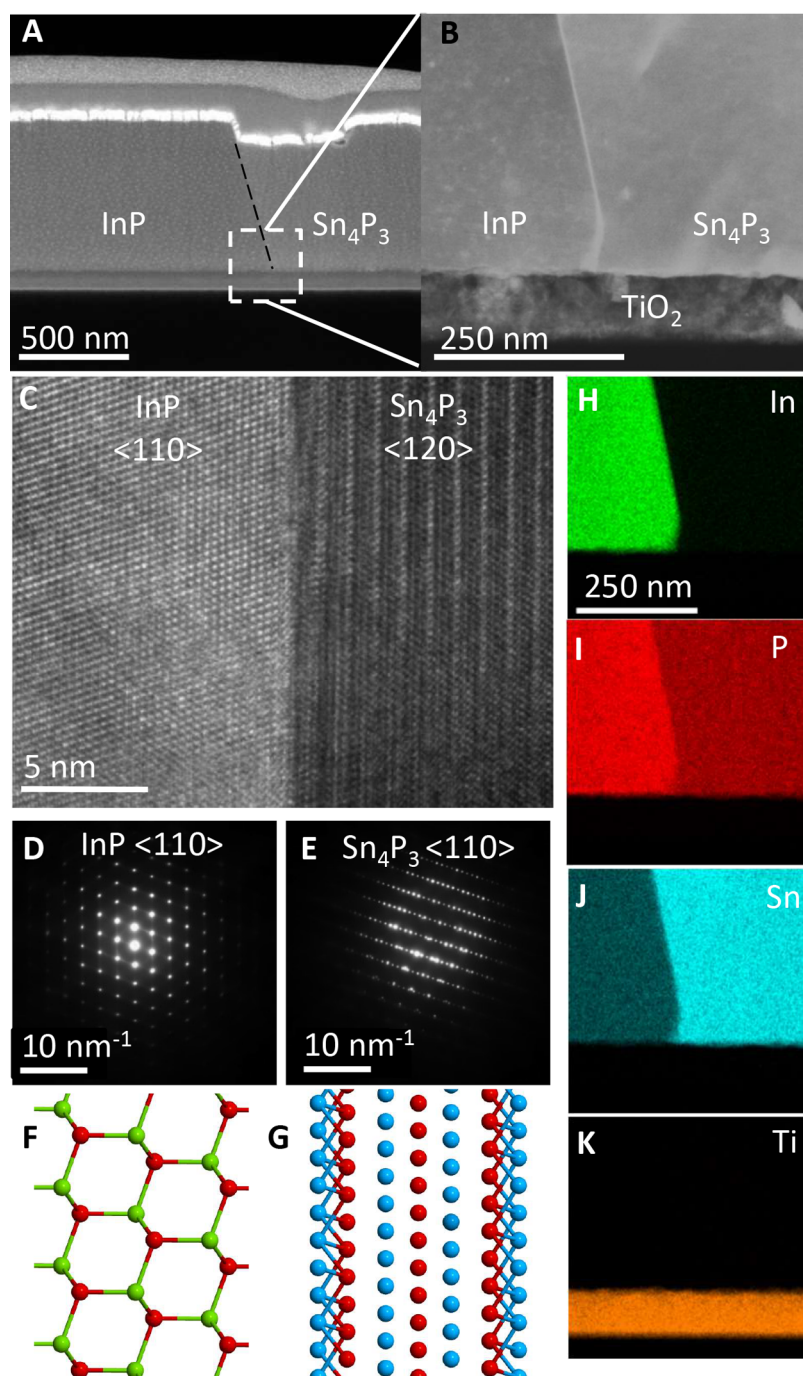


Figure 5. Lateral heterojunctions between dissimilar materials. (A) SEM image of an InP/Sn₄P₃ lateral heterojunction and (B) TEM image of the heterojunction and TiO₂ substrate. (C) High-resolution TEM image of the interface, showing nearly atomically sharp interface. SAED of (D) InP and (E) Sn₄P₃. Atomic scale model of (F) InP <110> with {111} termination and (G) Sn₄P₃ <120> with {100} termination at the interface. (H–K) EDS maps of In, P, Sn, and Ti, showing the heterojunction on the substrate clearly.

re-evaporation of the phosphorus from the liquid templates, reducing the supersaturation and the driving force for growth. Although In_xGa_{1-x}P is demonstrated here, a clear route is presented toward far-from-equilibrium growth of uniform ternary alloys with this growth technique.

Unlike III–V semiconductors explored here, many materials do not have well-established epitaxial substrates, limiting the ability to grow thin-film geometry single-crystalline materials. One example of this is tin phosphide, a promising emerging layered material system with multiple stable phases,^{25,26} each with dramatically different properties and crystal structures.

Rhombohedral Sn₄P₃²⁷ and hexagonal SnP^{28,29} have been recently demonstrated as ultra-high-capacity anode materials for sodium and lithium ion batteries, respectively. However, due to the lack of an available epitaxial template for tin phosphide, the demonstrations have been limited to powders, nanoparticles, and small bulk crystals.^{26–31} Nontemplated polycrystalline tin phosphide (Sn₄P₃ and SnP) microparticles grown on a Si/SiO₂ wafer and the corresponding X-ray diffraction spectra are shown in Figure S9. By removing the need for an epitaxial template, TLP enables us to grow phase-pure, templated crystalline Sn₄P₃ and SnP on a silicon/SiO₂

handle wafer. Growth is carried out by first depositing tin into circular arrays with a SiO_x capping layer, directly on the Si/SiO₂ or Mo substrate, and then following the TLP growth process to obtain tin phosphide. The atomic structures of rhombohedral Sn₄P₃³² and hexagonal SnP³³ are schematically shown in Figure 4A,B, respectively. Both phases exhibit a layered structure with alternating planes of P and Sn atoms along the *c*-axis, with Sn₄P₃ exhibiting seven alternating planes per layer and SnP exhibiting three. Figure 4C,D shows Raman spectra of Sn₄P₃ and SnP, respectively. Due to the dramatically different crystal structures, these materials have distinct Raman spectra, allowing us to identify the phase we have grown. When grown at 450 °C, 100% of the Raman spectra match that shown in Figure 4C, and at 550 °C, 100% match the spectra shown in Figure 4D. For growth temperatures within that range, both Raman spectra are observed, indicating that a combination of phases are present.

X-ray photoelectron spectroscopy (XPS) is used to then identify the valence states of the Sn and P atoms in both phases. Figure 4E shows the XPS spectra of tin (3d) in Sn₄P₃, illustrating the presence of only Sn⁴⁺ (487.6 eV). On the other hand, Figure 4F shows that in SnP a mixture of Sn⁴⁺ (487.6 eV) and Sn⁰ (485.3 eV) valences occurs. Figure 4G,H shows that both stoichiometries show the expected doublet phosphide P³⁻ (2p) peak (129.5 and 130.5 eV) and a phosphate PO^{x-} peak (134 eV). Survey scans showing the presence of only Sn_xP_y grown on Mo substrate are shown in Figure S10. The intensity of the phosphate peak was found to be higher on samples with longer exposure to ambient air after growth and is expected due to surface oxides (a similar phosphate PO^{x-} peak was also found to be present on the InP wafer, thus confirming this hypothesis, not shown here). Figure 4I1 shows an SEM image of tin phosphide templates grown on a Si/SiO₂ substrate and the corresponding EDS images showing tin (Figure 4I2), phosphorus (Figure 4I3), and Si (Figure 4I4). Figure 4J,K shows a high-resolution TEM image and selective area electron diffraction (SAED), respectively, of SnP, indicating the distinct single-crystalline nature of the grown material, as expected from the observed crystals during partial growth (representative SEM image shown in Figure S11).

Finally, we demonstrate that this approach enables high-quality heterointerfaces between non-epitaxial crystalline materials, which is not possible with vapor-phase epitaxy techniques. To achieve this, we heat an array of indium and tin mesas to 550 °C and then introduce phosphine. At these temperatures, the two metals will fully mix before introduction of PH₃. However, indium phosphide and tin phosphide do not form any stable ternary compound,³⁴ as the crystal structures are vastly dissimilar, thus both indium phosphide and tin phosphide grow from a single In/Sn melt. Figure 5A shows an SEM image of the InP–Sn₄P₃ crystals grown on a layer of atomic layer deposited TiO₂ on Si/SiO₂ handle wafer. Figure 5B shows a TEM image of the InP–Sn₄P₃ interface on the TiO₂ surface. High-resolution TEM imaging (Figure 5C) shows that this approach enables us to create *lateral atomically sharp crystalline heterostructures* from materials with completely dissimilar crystal structures. The SAED patterns of the InP and Sn₄P₃ crystals along the ⟨110⟩ axis are shown in Figure 5D,E, respectively. To gain an atomic scale understanding of the interface, we have indexed the TEM images of the InP and Sn₄P₃ to determine the orientation of both crystals at the interface. It is found that Sn₄P₃ (001) planes grow on top of an InP (111) termination. From this, we have built a ball-and-stick

chemical model of the InP (Figure 5F) and Sn₄P₃ (Figure 5G) showing the {111}InP||{001}Sn₄P₃||{110}InP||{120} Sn₄P₃ interfacial relationship.

Four EDS elemental maps of Figure 5B allow us to investigate materials and interface properties: In (Figure 5H), P (Figure 5I), Sn (Figure 5J), and Ti (Figure 5K). In Figure 5H, we observe a clear interface between the InP, Sn₄P₃, and underlying TiO₂, and Figure 5I shows P observed uniformly across both InP and Sn₄P₃. Due to the solubility of Sn in InP, we observe a background concentration of Sn doping in the InP (Figure 5J). The underlying TiO₂ substrate (Figure 5K) shows no In, P, or Sn incorporation due to the thermal stability at the growth temperatures. At these growth conditions, InP nucleates and grows first, incorporating Sn, and leaving behind a melt of Sn, after which Sn₄P₃ nucleates and grows. This can be predicted from the metal-rich liquidus curves of the In–P and Sn–P binary phase diagrams. At 550 °C, the solubility of P in liquid indium is <0.2%,³⁵ whereas the solubility of P in Sn is >10%.²⁵ Thus, as the concentration of P increases in the uniform Sn/In melt, the Gibbs free energy for InP precipitation will cause nucleation of the InP first. After this, the surface of the growing InP crystal will act as a sink for P atoms, depleting the entire template, suppressing further nucleation of InP and Sn₄P₃. After the InP crystal has consumed the excess In, the melt is expected to be entirely Sn with In impurities, and the phosphorus concentration will continue to increase. Finally, the Sn₄P₃ will nucleate and grow in the template, creating a lateral heterostructure as shown here. As this requires the two materials to have crystal structures so vastly dissimilar that the formation of any alloys is precluded, the set of high-quality material interfaces that can be formed with this approach is orthogonal to standard vapor-phase growth approaches.

CONCLUSION

A thermodynamic model of confined liquid metal wetting is developed, illustrating that a geometric condition exists such that liquid metal templates may be created on any substrate. With this, templated liquid-phase growth of crystalline InP, In_xGa_{1-x}P, and tin phosphide on non-epitaxial substrates is demonstrated. Through detailed optoelectronic characterization, it is shown that InP with excellent optoelectronic properties is obtained on a variety of substrates. By using far-from-equilibrium growth, uniform growth of ternary alloy semiconductors is observed despite being thermodynamically unfavorable. With tin templates, two distinct phases of tin phosphide are grown on amorphous substrates with full control over the phase purity. Finally, an atomically sharp lateral heterojunction between two materials with completely different crystal structures, InP and Sn₄P₃, was demonstrated.

The TLP growth platform enables the integration of high-performance electronic and photonic materials bypassing the need for an epitaxial template. Next generation neuromorphic computing, Internet of Things, photonic integrated circuits, and 3D integration all require multiple high-performance layers of devices. As traditional vapor-phase epitaxy cannot be used to directly create multiple layers of devices, TLP growth enables device integration at the microscale with crystalline materials. This would enable superior architectures as compared to the present integration techniques, which enable either coarse integration through physical stacking or integration with lower performance nanomaterials. For materials synthesis, TLP enables crystalline material development directly on the desired substrates, without the need for the development of an epitaxial

single-crystal substrate technology. Furthermore, a class of atomic-scale crystalline interfaces between materials with no epitaxial relation can be created, potentially impacting thermal, electronic, and photonic devices.

METHODS

Templated Liquid-Phase Growth. Each substrate was cleaned with acetone, isopropyl alcohol, and deionized water, blow-dried with dry nitrogen, and then photolithographically patterned with the desired templates. Indium (99.99995%) and/or tin (99.9999%) and/or gallium (99.99995%) was thermally evaporated on the lithographically patterned samples mounted on a cryo-cooled (liquid nitrogen) stage using an alumina-covered tungsten boat at rates of 4–5 Å/s. The thickness of evaporated metal was varied between 400 and 800 nm as required by the lateral mesa dimension and substrate based on the *thermodynamically controlled geometric wetting* model. A capping layer of 180–200 nm SiO₂ was electron-beam evaporated using SiO₂ pellets (99.99% pure, Kurt J. Lesker). This was followed by a standard photoresist lift-off procedure in acetone, resulting in templates of metal/capping layer stacks on the substrate.

TLP growth was done in a single-zone hot-wall tube furnace (Lindberg Blue) under a furnace temperature ranging between 450 and 650 °C (specific temperatures are mentioned in the main text for individual material systems). PH₃ (99.9995%, Matheson) was used as the P precursor, diluted with 99.999% H₂ to achieve the desired PH₃ partial pressure. The PH₃ flux was controlled to ensure nucleation of a single compound semiconductor crystal in each liquid metal template. This occurs by obtaining a *phosphorus depletion region* around the initial nucleation region, which prevents the surrounding liquid melt from being supersaturated with P, and thus no further stable nucleation occurs in that region. This allows the initial nucleus to grow out into a single crystal, consuming the entire metal template.

Scanning Electron Microscopy. Scanning electron microscopy images were obtained using either a Hitachi S4800 or JEOL JSM-7001F field-emission scanning electron microscope. An energy-dispersive X-ray spectrometer detector attached to the JEOL JSM-7001F was also used to collect SEM EDS spectra and maps.

Transmission Electron Microscopy. Scanning transmission electron microscopy images and selective area electron diffraction patterns were obtained using either a JEOL JEM-2100F (200 kV) or FEI Titan (300 kV) instrument. An energy-dispersive X-ray spectrometer detector attached to the JEOL JEM-2100F was also used to collect S/TEM EDS spectra and maps.

Optical Microscopy. Optical micrographs were obtained from a Nikon Eclipse L150 optical microscope connected to a Pixelink CCD camera.

X-ray Photoelectron Spectroscopy. X-ray photoelectron spectra were obtained using a Kratos Axis Ultra spectrometer equipped with a monochromated Al anode operating at 60 W. All spectra were referenced to the adventitious carbon peak at 284.8 eV. Referencing and peak fitting were done using CasaXPS software.

X-ray Diffraction. X-ray diffraction spectra were collected on a Bruker-AXS D8 X-ray diffractometer equipped with a GADDS area detector and operated at 35 kV and 40 mA with a Co K α of 1.79 Å collimated to a 0.8 mm spot size.

Photoluminescence and Raman Spectra Measurement. Steady-state photoluminescence measurements and Raman spectroscopy were carried out in a Renishaw inVia confocal Raman microscope setup using a constant-power 532 nm laser source as the excitation and a Si CCD detector. ND filter arrays were used to tune the power incident on the sample for obtaining PL data over a wide range of incident powers. The comparison InP was a 100-oriented wafer with a reported doping concentration of $\sim 10^{17}$ cm⁻³.

Urbach Parameter Estimation. The van Roosbroeck–Shockley equation relates the optical emission rate per unit energy $R(h\nu)$ to the absorption coefficient $\alpha(h\nu)$ as²⁰

$$R(h\nu) = \alpha(h\nu) \frac{8\pi\nu^2 n^2}{hc^2 (e^{h\nu/kT} - 1)}$$

where $R(h\nu)$ is the emission intensity, ν is frequency, h is Planck's constant, c is the speed of light in vacuum, k is Boltzmann's constant, and T is absolute temperature.

Energies for which the absorption coefficient is small, such as in the band gap, the (external) photoluminescence spectrum $P(h\nu)$ may be approximated to be of similar shape to that of the emission spectrum, irrespective of the thickness of the sample. Thus, the van Roosbroeck–Shockley equation may be represented as²¹

$$\alpha(h\nu) \propto P(h\nu) \frac{(e^{h\nu/kT} - 1)}{n^2 (h\nu)^2}$$

As first pointed out by Franz Urbach, the absorption coefficient in the band gap scales exponentially with energy,¹⁹ so that it can be fitted with an equation of the form

$$\alpha(h\nu) = \alpha_0 e^{(E - E_{\text{ref}})/E_0}$$

where α_0 and E_0 are fitting parameters and E_{ref} is a reference energy. The term E_0 is referred to as Urbach parameter and is indicative of the sharpness of the exponentially decreasing absorption in the band gap.

Though it is not well understood, it is thought that the absorption in the band gap is related to band gap states arising from intrinsic and extrinsic crystal defects, and thus a lower value of Urbach parameter is a measure of lesser defect density in the material.

Photoluminescence External Quantum Efficiency. A broadband light source with calibrated relative intensity variation was used to obtain the system response function, η_{sys} . A wavelength calibrated power meter Thorlabs PM100D was used to measure the incident laser powers and calculate the excitation photon flux, R_{exc} (number of photons/area/s). The reference InP wafer photoluminescence with known quantum efficiency (at a given incident power) was thereby used to calibrate the instrument counts to external photon emission flux R_{PL} (number of photons/area/s).

The external luminescence efficiency of the grown InP was thus calculated from the measured photoluminescence as

$$\eta_{\text{ext}} = \frac{R_{\text{PL}}}{R_{\text{exc}}}$$

where R_{PL} is the photoluminescence flux and R_{exc} is the incident photon flux.

Calculation of Quasi-Fermi Level Splitting. The quasi-Fermi level splitting is calculated as³⁶

$$\Delta E_{\text{F}} = kT \ln \left(\frac{R_{\text{abs}}}{\int_0^{2\pi} \int_0^{\pi/2} \int_{-\infty}^{\infty} a(E, \theta) b(E) \cos(\theta) dE d\theta d\phi} \right) + kT \ln(\eta_{\text{ext}})$$

where η_{ext} is the photoluminescence external quantum efficiency and $a(E, \theta)$ is the effective absorbance of the incident flux by the semiconductor, given as

$$a(E, \theta) = \mathbb{A}(E) \times \mathbb{T}(\theta)$$

The energy-dispersive absorbance $\mathbb{A}(E)$ of the semiconductor of thickness L is

$$\mathbb{A}(E) = 1 - e^{-2\alpha(E)L}$$

with the absorption coefficient

$$\alpha(E) = \begin{cases} 10^4 \text{ cm}^{-1} & \text{for } E \geq E_{\text{g}} \\ 10^4 \times e^{E - E_{\text{g}}/E_0} \text{ cm}^{-1} & \text{for } E \leq E_{\text{g}} \end{cases}$$

where E is the photon energy, E_{g} is the band gap energy, and E_0 is the Urbach parameter.

It may be noted that the absorbance thus calculated assumes a perfect reflector at the bottom of the InP, which may not be true in these substrates.

$\Delta(\theta)$ is the transmittance of the semiconductor–air interface calculated from Fresnel equations; $b(E)$ is the blackbody spectrum at temperature T given by

$$b(E) = \frac{2n^2}{h^3c^2} E^2 \left(\frac{1}{e^{E/kT} - 1} \right)$$

where n is the refractive index of free space, h is Planck's constant, c is the speed of light in vacuum, k is Boltzmann's constant, and T is temperature (here taken to be 300 K). R_{abs} is the absorbed photon flux calculated as

$$R_{\text{abs}} = a(E_{\text{exc}}, \theta) \times R_{\text{exc}}$$

with E_{exc} being the laser excitation energy, and $\theta = 0$ for normal incidence of the excitation.

Crystal Structure Rendering. Ball-and-stick three-dimensional models of crystal structures were built using the Crystal Builder module in Atomistix ToolKit (ATK) Virtual NanoLab (VNL). Crystallographic Information Framework (CIF) files from the Inorganic Crystal Structure Database (ICSD) were directly read by the Builder module to obtain the unit cell information, which was rendered in a 3D ball-and-stick representation.

ASSOCIATED CONTENT

Supporting Information

The Supporting Information is available free of charge on the ACS Publications website at DOI: 10.1021/acsnano.8b01819.

Thermodynamic modeling of geometric structures is discussed in detail; optical microscope images of uncontrolled dewetted InP growth (Figure S1); optical microscope images of evaporated In or Sn patterns of different radii on the substrate (Figure S2); optical microscope images showing wetting characteristics of In on TiO₂ and Si₃N₄ (Figure S3); optical microscope images showing wetting characteristics of Sn on TiO₂ and SiO₂ (Figure S4); wetting characteristics of In on MoO_x compared to Gd₂O₃ (Figure S5); representative PL spectra of TLP InP grown on different substrates is compared with InP wafer (Figure S6); characteristics of TLP growth on Mo (Figure S7); Raman spectrum of GaP grown on Si/SiO₂ (Figure S8); optical microscope images and powder XRD scans of nontemplated microcrystalline tin phosphide microparticles grown on Si/SiO₂ substrate (Figure S9); XPS survey scans of tin phosphide on Mo substrate (Figure S10); SEM image of large-area single-crystal of hexagonal SnP growing on SiO₂ (Figure S11); comparison of PL spectral metrics of InP grown on different substrates with InP wafer (Table S1) (PDF)

AUTHOR INFORMATION

Corresponding Author

*E-mail: rkapadia@usc.edu.

ORCID

Debarghya Sarkar: 0000-0002-5411-7066

Wei Wang: 0000-0001-7007-0088

Han Wang: 0000-0001-5121-3362

Stephen B. Cronin: 0000-0001-7089-6672

Rehan Kapadia: 0000-0002-7611-0551

Author Contributions

D.S., W.W., and R.K. designed the experiments. D.S. and W.W. performed the growths. D.S., W.W., L.B., and H.Z. carried out optoelectronic characterization. D.S., C.R., Q.L., and H.S. carried out sample fabrication. D.S., R.K., and M.L. developed

the thermodynamic wetting model. M.M. performed the TEM sample preparation and imaging. D.S., A.J.C., and H.S. performed the XPS spectroscopy. D.S., M.Y., and S.N. performed XRD spectroscopy. D.S., W.W., M.M., A.C., C.R., L.B., H.W., S.B.C., J.R., M.L., and R.K. analyzed the data. D.S. and R.K. wrote the paper, and all authors contributed in editing the paper.

Notes

The authors declare no competing financial interest.

ACKNOWLEDGMENTS

R.K. acknowledges funding from the National Science Foundation (Award No. 1610604), NASA/JPL (Award No. 1571721), and Semiconductor Research Corporation (Award No. 2018-NM-2799). D.S. thanks the support by the USC Annenberg Graduate Fellowship. The authors acknowledge the Center for Electron Microscopy and Microanalysis at USC and the Molecular Foundry at Lawrence Berkeley National Laboratory, a user facility supported by the Office of Science, Office of Basic Energy Sciences of the U.S. Department of Energy (DOE) under Contract No. DE-AC02-05CH11231. This research was supported in part by Army Research Office (ARO) Award No. W911NF-14-1-0228 (H.S.) and Department of Energy (DOE) Award No. DE-FG02-07ER46376 (S.B.C.). J.R. acknowledges USC Viterbi School of Engineering Startup Funds and support from the Air Force Office of Scientific Research under Award No. FA9550-16-1-0335. S.N. acknowledges Link Foundation Energy Fellowship.

REFERENCES

- (1) Del Alamo, J. A. Nanometre-Scale Electronics with III-V Compound Semiconductors. *Nature* **2011**, *479*, 317–323.
- (2) Gudiksen, M. S.; Lauen, L. J.; Wang, J.; Smith, D. C.; Lieber, C. M. Growth of Nanowire Superlattice Structures for Nanoscale Photonics and Electronics. *Nature* **2002**, *415*, 617–620.
- (3) Liang, D.; Bowers, J. E. Recent Progress in Lasers on Silicon. *Nat. Photonics* **2010**, *4*, 511–517.
- (4) Chen, S.; Li, W.; Wu, J.; Jiang, Q.; Tang, M.; Shutts, S.; Elliott, S. N.; Sobiesierski, A.; Seeds, A. J.; Ross, I.; et al. Electrically Pumped Continuous-Wave III–V Quantum Dot Lasers on Silicon. *Nat. Photonics* **2016**, *10*, 307–311.
- (5) Morales, A. M.; Lieber, C. M. A Laser Ablation Method for the Synthesis of Crystalline Semiconductor Nanowires. *Science* **1998**, *279*, 208–211.
- (6) Duan, X.; Huang, Y.; Cui, Y.; Wang, J.; Lieber, C. M. Indium Phosphide Nanowires As Building Blocks for Nanoscale Electronic and Optoelectronic Devices. *Nature* **2001**, *409*, 66–69.
- (7) Kuykendall, T.; Ulrich, P.; Aloni, S.; Yang, P. Complete Composition Tunability of InGaN Nanowires Using a Combinatorial Approach. *Nat. Mater.* **2007**, *6*, 951–956.
- (8) Tomioka, K.; Yoshimura, M.; Fukui, T. A III-V Nanowire Channel on Silicon for High-Performance Vertical Transistors. *Nature* **2012**, *488*, 189–192.
- (9) Ko, H.; Takei, K.; Kapadia, R.; Chuang, S.; Fang, H.; Leu, P. W.; Ganapathi, K.; Plis, E.; Kim, H. S.; Chen, S.-Y.; et al. Ultrathin Compound Semiconductor on Insulator Layers for High-Performance Nanoscale Transistors. *Nature* **2010**, *468*, 286–289.
- (10) Yablonovitch, E.; Hwang, D.; Gmitter, T.; Florez, L.; Harbison, J. Van Der Waals Bonding of GaAs Epitaxial Liftoff Films onto Arbitrary Substrates. *Appl. Phys. Lett.* **1990**, *56*, 2419–2421.
- (11) Yoon, J.; Jo, S.; Chun, I. S.; Jung, I.; Kim, H.-S.; Meitl, M.; Menard, E.; Li, X.; Coleman, J. J.; Paik, U.; et al. GaAs Photovoltaics and Optoelectronics Using Releasable Multilayer Epitaxial Assemblies. *Nature* **2010**, *465*, 329–333.
- (12) Justice, J.; Bower, C.; Meitl, M.; Mooney, M. B.; Gubbins, M. A.; Corbett, B. Wafer-Scale Integration of Group III-V Lasers on Silicon

Using Transfer Printing of Epitaxial Layers. *Nat. Photonics* **2012**, *6*, 610–614.

(13) Chen, K.; Kapadia, R.; Harker, A.; Desai, S.; Kang, J. S.; Chuang, S.; Tosun, M.; Sutter-Fella, C. M.; Tsang, M.; Zeng, Y.; et al. Direct Growth of Single-Crystalline III–V Semiconductors on Amorphous Substrates. *Nat. Commun.* **2016**, *7*, 10502.

(14) Kapadia, R.; Yu, Z.; Wang, H.-H. H.; Zheng, M.; Battaglia, C.; Hettick, M.; Kiriya, D.; Takei, K.; Lobaccaro, P.; Beeman, J. W.; et al. A Direct Thin-Film Path Towards Low-Cost Large-Area III-V Photovoltaics. *Sci. Rep.* **2013**, *3*, 2275.

(15) Lin, Q.; Sarkar, D.; Lin, Y.; Yeung, M.; Blankemeier, L.; Hazra, J.; Wang, W.; Niu, S.; Ravichandran, J.; Fan, Z.; et al. Scalable Indium Phosphide Thin-Film Nanophotonics Platform for Photovoltaic and Photoelectrochemical Devices. *ACS Nano* **2017**, *11*, 5113–5119.

(16) Wang, H.-P.; Sutter-Fella, C. M.; Lobaccaro, P.; Hettick, M.; Zheng, M.; Lien, D.-H.; Miller, D. W.; Warren, C. W.; Roe, E. T.; Lonergan, M. C.; et al. Increased Optoelectronic Quality and Uniformity of Hydrogenated p-InP Thin Films. *Chem. Mater.* **2016**, *28*, 4602–4607.

(17) Kapadia, R.; Yu, Z.; Hettick, M.; Xu, J.; Zheng, M. S.; Chen, C.-Y.; Balan, A. D.; Chrzan, D. C.; Javey, A. Deterministic Nucleation of InP on Metal Foils with the Thin-Film Vapor–Liquid–Solid Growth Mode. *Chem. Mater.* **2014**, *26*, 1340–1344.

(18) Sarkar, D.; Tao, J.; Wang, W.; Lin, Q.; Yeung, M.; Ren, C.; Kapadia, R. Mimicking Biological Synaptic Functionality with an Indium Phosphide Synaptic Device on Silicon for Scalable Neuro-morphic Computing. *ACS Nano* **2018**, *12*, 1656–1663.

(19) Urbach, F. The Long-Wavelength Edge of Photographic Sensitivity and of the Electronic Absorption of Solids. *Phys. Rev.* **1953**, *92*, 1324.

(20) Van Roosbroeck, W.; Shockley, W. Photon-Radiative Recombination of Electrons and Holes in Germanium. *Phys. Rev.* **1954**, *94*, 1558.

(21) Kost, A.; Lee, H. C.; Zou, Y.; Dapkus, P. D.; Garmire, E. Band-Edge Absorption Coefficients from Photoluminescence in Semiconductor Multiple Quantum Wells. *Appl. Phys. Lett.* **1989**, *54*, 1356–1358.

(22) Kato, T.; Matsumoto, T.; Ogura, H. Liquid Phase Epitaxy of InGaP on GaAs (100) Substrates at Low Growth Temperatures Down to 630° C. *Jpn. J. Appl. Phys.* **1990**, *29*, L856.

(23) Hakkı, B. W.; Jayaraman, A.; Kim, C. K. Band Structure of InGaP from Pressure Experiments. *J. Appl. Phys.* **1970**, *41*, 5291–5296.

(24) Kato, T.; Matsumoto, T.; Ishida, T. Raman Spectral Behavior of In_{1-x}Ga_xP (0 < x < 1). *Jpn. J. Appl. Phys.* **1988**, *27*, 983.

(25) Ritscher, A.; Schmetterer, C.; Ipsier, H. Pressure Dependence of the Tin–Phosphorus Phase Diagram. *Monatsh. Chem.* **2012**, *143*, 1593–1602.

(26) Tallapally, V.; Esteves, R. J. A.; Nahar, L.; Arachchige, I. U. Multivariate Synthesis of Tin Phosphide Nanoparticles: Temperature, Time, and Ligand Control of Size, Shape, and Crystal Structure. *Chem. Mater.* **2016**, *28*, 5406–5414.

(27) Lan, D.; Wang, W.; Shi, L.; Huang, Y.; Hu, L.; Li, Q. Phase Pure Sn₄P₃ Nanotops by Solution-Liquid-Solid Growth for Anode Application in Sodium Ion Batteries. *J. Mater. Chem. A* **2017**, *5*, 5791–5796.

(28) Kim, Y.; Hwang, H.; Yoon, C. S.; Kim, M. G.; Cho, J. Reversible Lithium Intercalation in Teardrop-Shaped Ultrafine SnP_{0.94} Particles: An Anode Material for Lithium-Ion Batteries. *Adv. Mater.* **2007**, *19*, 92–96.

(29) Aso, K.; Kitaura, H.; Hayashi, A.; Tatsumisago, M. SnP_{0.94} Active Material Synthesized in High-Boiling Solvents for All-Solid-State Lithium Batteries. *J. Ceram. Soc. Jpn.* **2010**, *118*, 620–622.

(30) Zaikina, J. V.; Kovnir, K. A.; Sobolev, A. N.; Presniakov, I. A.; Kytin, V. G.; Kulbachinskii, V. A.; Olenev, A. V.; Lebedev, O. I.; Tendeloo, G. V.; Dikarev, E. V.; et al. Highly Disordered Crystal Structure and Thermoelectric Properties of Sn₃P₄. *Chem. Mater.* **2008**, *20*, 2476–2483.

(31) Ganesan, R.; Richter, K. W.; Schmetterer, C.; Effenberger, H.; Ipsier, H. Synthesis of Single-Phase Sn₃P₄ by an Isopiestic Method. *Chem. Mater.* **2009**, *21*, 4108–4110.

(32) Olofsson, O.; Aava, U.; Haaland, A.; Resser, D.; Rasmussen, S. E.; Sunde, E.; Sorensen, N. A. X-Ray Investigation of the Tin-Phosphorus System. *Acta Chem. Scand.* **1970**, *24*, 1153–1162.

(33) Gullman, J. The Crystal Structure of SnP. *J. Solid State Chem.* **1990**, *87*, 202–207.

(34) In-P-Sn Vertical Section of Ternary Phase Diagram: Datasheet from “Pauling File Multinaries Edition–2012”; In *SpringerMaterials*; Springer-Verlag Berlin Heidelberg & Material Phases Data System (MPDS): Berlin, 2012; http://Materials.Springer.Com/Isp/Phase-Diagram/Docs/C_1401076.

(35) Panish, M. B. A. Thermodynamic Evaluation of the Simple Solution Treatment of the Ga-P, In-P and Ga-As Systems. *J. Cryst. Growth* **1974**, *27*, 6–20.

(36) Miller, O. D.; Yablonoitch, E.; Kurtz, S. R. Strong Internal and External Luminescence as Solar Cells Approach the Shockley–Queisser Limit. *IEEE J. Photovoltaics* **2012**, *2*, 303–311.